

# Halo structure, masses of dark objects and parallax microlensing

D. Marković

*Theoretical Astrophysics Center, Juliane Maries Vej 30, DK-2100 Copenhagen Ø, Denmark* <sup>★</sup>  
*draza@tac.dk*

10 August 1997

## ABSTRACT

We study the use of parallax microlensing to separate the effects of the mass function of dark massive halo objects (MHOs or ‘machos’) on the one hand and their spatial distribution and kinematics on the other. This disentanglement is supposed to allow a much better determination of the two than could be achieved entirely on the basis of the durations of events. We restrict our treatment to the same class of power-law spherical models for the halo of MHOs studied in a previous paper (Markovic & Sommer-Larsen 1997). Whereas the duration-based error in the average MHO mass,  $\bar{\mu} \equiv \bar{M}/M_\odot$  exceeds (at  $N = 100$  events)  $\bar{\mu}$  by a factor of 2 or more, parallax microlensing remarkably brings it down to 15-20% of  $\bar{\mu}$ , regardless of the shape of the mass function. In addition, the slope  $\alpha$  of the mass function,  $dn/d\mu \propto \mu^\alpha$ , can be inferred relatively accurately ( $\sigma_\alpha < 0.4$ ) for a broader range,  $-3 < \alpha < 0$ . The improvement in the inference of the halo structure is also significant: the index  $\gamma$  of the density profile ( $\rho \sim R^{-\gamma}$ ) can be obtained with the error  $\sigma_\gamma < 0.4$ . While in a typical situation the errors for the parameters specifying the velocity dispersion profile are of about the same magnitude as the parameters, virtually all the uncertainty is ‘concentrated’ in linear combinations of the parameters that may have little influence on the profile and thus allow its reasonably accurate inference.

**Key words:** Microlensing – Galactic halo – Macho mass function.

## 1 INTRODUCTION AND OVERVIEW

A statistical analysis by Alcock *et al.* (1996) of the 2-year microlensing data (6 or 8 events) obtained by the MA-CHO project in the direction of the Large Magellanic Cloud (LMC) indicated that the massive dark halo objects (MHOs or ‘machos’) responsible for the microlensing events could account for 30-100% of the total mass in the halo of our Galaxy. According to their analysis, typical (average) mass of the MHOs should lie in the range  $0.1 - 0.6 M_\odot$ . The more recent 4-year data (14 events, Axelrod 1997) yield similar ranges of the inferred quantities. Apart from the statistical error due to the relatively small number of events, our ignorance regarding the structure of the halo of massive objects (i.e., their spatial distribution and kinematics) leads to rather large uncertainties in the inferred masses.

This last source of error is not likely to be extinguished if one relies only on the measurement of event durations  $T = R_E/v_n$  ( $R_E$  is the Einstein radius,  $v_n$  is the MHO’s

velocity orthogonal to the line of sight). Indeed, as shown by Markovic & Sommer-Larsen (1997, paper I), for the number of events  $N < 1000$  the halo structure cannot be constrained sufficiently to allow a determination of the average mass  $\bar{\mu} \equiv \bar{M}/M_\odot$  of the MHOs to better than a factor of about 2. Furthermore, paper I discussed only a limited class of spherical haloes; the results of Evans (1997), based on a far wider variety of halo models, imply that the range of  $\bar{\mu}$  (at virtually arbitrary  $N$ ) could in principle extend from 0.1 to 1.

The duration  $T$  is, however, not the only relevant quantity that can be obtained from a microlensing event. For instance, photometric (Gould 1994a; Nemiroff & Wickramasinghe 1994) or spectroscopic (Maoz & Gould 1994) methods have been proposed to measure the proper motion of the lens  $\mathbf{v}_n/zD$ , where  $D$  is the Earth-source distance,  $z \equiv D_L/D$  and  $D_L$  is the Earth-lens distance. Another approach [discussed by Grieger, Kayser & Refsdal (1986) in the context of quasar astronomy] is parallax microlensing, i.e., observing magnification through telescopes displaced from each other by about 1AU. More recently, Gould (1994b) studied and advocated the use of parallax microlensing to obtain more in-

<sup>★</sup> Address after September 1st, 1997: Department of Physics, University of Illinois at Urbana-Champaign, 1110 W. Green St., Urbana, IL 61801, USA

formation regarding the position and velocities of the lenses (and consequently reduce the uncertainty of their masses).

The utility of the parallaxes stems primarily from the fact that the delay  $\tau$  between the maximal magnifications in the two detectors (one on the Earth and the other on a satellite in a heliocentric orbit) does not depend on the mass of the MHO crossing the two lines of sight to a source. Additional information is contained in the two maximal magnifications determined by the impact parameters  $u_1$  and  $u_2$  measured in units of the Einstein radius. Breaking a 4-fold degeneracy (Gould 1994b; see also Section 2 of the present paper) by observing from a second satellite would allow us to obtain the so-called reduced transverse velocity  $\tilde{\mathbf{v}} \equiv \mathbf{v}_n/(1-z)$  of the MHO. A sufficiently large number of such measurements would then presumably put tight constraints on the structure of the halo. However, even in absence of a second satellite, the relative motion of the first satellite and the Earth could suffice to reduce the ambiguity to (at most) a 2-fold degeneracy in the direction of  $\tilde{\mathbf{v}}$  for a majority of events (Gould 1995; Bouteux & Gould 1996). [According to Han & Gould (1995) this should (in the case of galactic bulge microlensing) permit measurement of *individual* MHO masses to an accuracy of about 0.2 on the logarithmic scale.]

In this paper we explore quantitatively the extent to which one could expect parallax microlensing to help constrain the mass function of the MHOs as well as their spatial distribution and kinematics. The assumptions of the present paper are similar to those of paper I: for convenience we again limit ourselves to a class of spherical halo models (see section 3) described by a set of 5 parameters (the singular isothermal sphere is a particularly simple member of this class). On the other hand, the mass function is assumed to be a simple power law,  $dn/d\mu \propto \mu^\alpha$  characterised by three parameters (independent of the position in the halo): the average mass  $\mu$ , slope  $\alpha$  and range  $\beta$  on the logarithmic scale.

Although lacking somewhat in generality, this framework will allow a straightforward application of the apparatus of statistical parameter estimation: the errors of maximum likelihood inference of the mass function and halo parameters can be estimated from the sensitivity of the distributions of directly measurable quantities to small shifts in the underlying parameters (see paper I and Section 5 of the present paper). We call such estimates the Cramer errors (Cramer 1946). For simplicity we will study both the *degenerate* (with the full 4-fold degeneracy) parallax microlensing, where the observable quantities are  $T$ ,  $p \equiv \tau/T$ ,  $u_1$  and  $u_2$  and *resolved* (the 4-fold degeneracy completely removed) parallax microlensing with observables  $T$ ,  $p$  and  $w = \sqrt{a^2 - p^2}$ , where  $a$  is the transversal distance between the two lines of sight in the lens plane measured in Einstein radii.

In specific computations we at first adopt for the parameters of the underlying halo model the values corresponding to the centrally condensed ( $\gamma = 3.4$ ;  $\rho \propto R^{-\gamma}$ ;  $R$  is the distance from the centre of the Galaxy) halo of blue horizontal branch field stars (BHBFS; see Section 3). Although one might speculate as to the relevance — or irrelevance — of this structure to the halo of MHOs (paper I), these values are simply taken as a convenient starting point for our

numerical experiment and the accuracy of their inference is estimated. In addition we briefly discuss the inference starting from the singular isothermal sphere ( $\gamma = 2$ ; constant, isotropic velocity dispersion) as a model for the MHO halo.

We find that parallax microlensing reduces the Cramer errors in  $\bar{\mu}$  from a factor of 2-10, characteristic of measurements of event durations, to only 15-20% (at  $N = 100$  events) for *a priori* unknown halo structure parameters. This error is typical of inference under the (unrealistic) assumption that the halo model *is* accurately known *a priori* and is kept fixed in the maximum-likelihood fitting of the distribution of measurable quantities. The improvement indeed results from an effective disentanglement of the mass function from the halo structure. In addition, while parallax-based errors in parameters  $\alpha$  and  $\beta$ , specifying the shape of the mass function, are comparable to duration-based errors if  $\alpha$  is sufficiently close to -1.5, the growth of the errors away from this value is strongly restrained by the parallaxes (see Fig. 10).

Parallax microlensing also reduces by about two orders of magnitude the Cramer errors for the halo parameters. The power index  $\gamma$  of the halo density profile is determined with the error  $\sigma_\gamma < 0.4$  (at both  $\gamma = 3.4$  and  $\gamma = 2$ ), again from  $N = 100$  events. On the other hand, the errors in the parameters specifying the velocity dispersion profile are of roughly the same magnitude as the parameters themselves. This, however, does not necessarily mean that the profile will be poorly determined: as shown in Section 5, virtually all uncertainty (at  $\gamma = 3.4$ ) is due to the existence of a *single* linear combination of velocity dispersion parameters that is poorly constrained even by parallax microlensing. Indeed, small displacements in the parameter space along this vector cause a particularly weak change in the velocity profile. In addition, these changes tend to occur predominantly at large radii, where the microlensing rate is low. The peculiarities of the singular isothermal sphere, on the other hand, lead to the existence of *three* poorly constrained linear combinations of velocity dispersion parameters, none of them having a significant effect on the flat velocity profile. Remarkably, all the above conclusions are virtually independent of whether we use the degenerate or fully resolved parallaxes: the improvement due to resolving the degeneracy is modest.

In Section 2 of this paper we derive expressions for distribution functions of measurable quantities. These expressions are general and can be used with arbitrary halo models. The specific class of halo models used in this paper is described in Section 3 (following a similar section in paper I). Section 4 deals with the morphology of the distribution functions derived in Section 2, while Section 5 explores their sensitivity to the underlying parameters and thus derives the Cramer errors of inference. Finally, section 6 contains basic conclusions of this paper along with a bit of speculation regarding their more general validity.

## 2 DIFFERENTIAL PARALLAX MICROLENSING RATES

As observed from the Earth, a lens of mass  $M = \mu M_\odot$ , crossing the Earth-source line of sight at distance  $zD$  ( $0 \leq z \leq 1$ ) from the Earth and with the impact parameter  $u_1 R_E$  [ $R_E = r_E \sqrt{\mu} \sqrt{z(1-z)}$ ,  $r_E \equiv 2\sqrt{GM_\odot D/c^2} = 3.2 \times 10^9$  km]

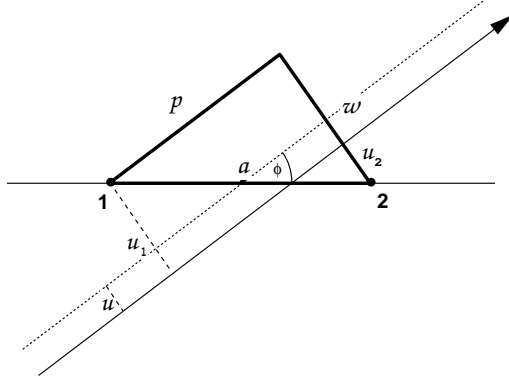


**Figure 1.** A parallax microlensing event projected onto the lens plane (orthogonal to the line of sight). All distances are given in units of the Einstein radius  $R_E$ .

will magnify the star by the maximum factor  $A_{\max} = (u_1^2 + 2)/(u_1\sqrt{u_1^2 + 4})$ . On the other hand, a satellite will detect maximum magnification, determined by the impact parameter  $u_2 R_E$  relative to the satellite-source line of sight, with the time shift  $\tau$  from the moment of the Earth-observed maximum magnification.

The geometric relations between the observable quantities,  $T \equiv R_E/v_n$  (event duration as observed by both the Earth-based observer and the satellite),  $\tau$ ,  $u_1$  and  $u_2$ , are easily derived from Fig. 1. If  $\mathbf{r}$  is the component of the Earth-satellite vector orthogonal to the line of sight, its source-centered projection onto the plane (also orthogonal to the line of sight) of the lens is

$$\mathbf{a} = \frac{\mathbf{r}(1-z)}{R_E} = \frac{\mathbf{r}}{r_E} \frac{1}{\sqrt{\mu}} \sqrt{\frac{1-z}{z}} \quad (1)$$

(measured in units of the Einstein radius  $R_E$ ).

The points ‘1’ and ‘2’ in Fig. 1 denote intersections of the Earth-source and satellite-source lines of sight respectively with the lens plane. The lens’ trajectory along the unit vector  $\hat{\mathbf{v}} = (\cos \phi, \sin \phi)$  (again, projected on the lens plane), shown as the solid arrow, crosses the 1-2 line at distance  $u R_E$  from the parallel line (dotted) drawn through the midpoint between 1 and 2. Consequently,

$$p \equiv a \cos \phi = \frac{r(1-z) \cos \phi}{v_n} \frac{1}{T} = \frac{\tau}{T} \quad (2)$$

is an observable quantity. On the other hand,  $w \equiv a \sin \phi$  generally cannot be obtained unambiguously from  $u_1$  and  $u_2$  only; the 4-fold degeneracy is illustrated in Fig. 2. A secure way of breaking this degeneracy would be to use a second satellite [the line tangent to three circles of radii  $u_1$ ,  $u_2$  and  $u_3$  (the last measured from the second satellite) is unique]. However, as Gould (1995) has shown, the motion of the Earth and the single satellite relative to the line of sight should allow us to resolve the ambiguity — at least regarding the magnitude of  $w$  — in most cases. Nevertheless, in this paper we will discuss both the ‘degenerate’ (the 4-fold ambiguity unresolved) and the ‘resolved’ ( $w$  uniquely determined) parallax microlensing.

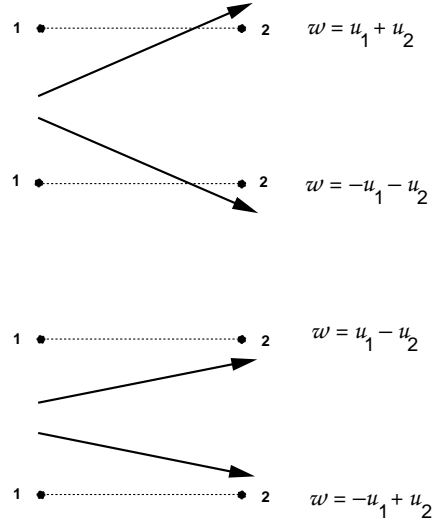


**Figure 2.** Four possibilities corresponding to a pair of values  $u_1 \geq 0$ ,  $u_2 \geq 0$  in the case of *degenerate* parallax microlensing.

The lens’ rate of crossing near the line of sight per single source and a single (number density near the Sun  $n_o = 1$ ) lens is

$$\Gamma = \int d\mu \frac{dn_o}{d\mu} \int DH(z) dz \int R_E(z) du \int f_n(v_n, \phi) v_n^2 dv_n d\phi, \quad (3)$$

where  $H(z)$  [ $H(0) = 1$ ] is the MHOs’ halo density profile along the line of sight,  $f_n$  [ $\int f_n(v_n, \phi) v_n dv_n d\phi = 1$ ] is the  $z$ -dependent, 2-dimensional distribution of velocities projected orthogonal to the line of sight and  $dn_o/d\mu$  [ $\int (dn_o/d\mu) d\mu = 1$ ] is the  $z$ -independent mass function of the MHOs.

Using

$$z = \frac{(r/r_E)^2}{\mu a^2 + (r/r_E)^2}, \quad (4)$$

rewriting the lens plane area element

$$dpdw = a da d\phi = \frac{1}{2} \left( \frac{dz}{da^2} \right)^{-1} dz d\phi, \quad (5)$$

and switching to integration over  $T$  ( $dv_n/dT = -v_n/T$ ) we obtain

$$\begin{aligned} \chi(T, p, w) &\equiv \frac{d\Gamma}{dT dp dw} \\ &= \int d\mu \frac{dn_o}{d\mu} DH(z) R_E(z) f_n(v_n, \phi) \frac{v_n^3}{T} \frac{2(r/r_E)^2 \mu}{[\mu a^2 + (r/r_E)^2]^2}, \end{aligned} \quad (6)$$

where  $v_n = r_E \sqrt{\mu} \sqrt{z(1-z)}/T$  and  $\tan \phi = w/p$ .

By contrast with resolved parallaxes, where  $\chi(T, p, w)$  is of more immediate relevance, measuring  $u_1 = |u + w/2|$  and  $|u - w/2|$  (see Fig. 1) is not sufficient to uniquely determine  $w$  in the case of degenerate parallaxes. Inserting ‘dummy’ integration  $\int du_1 \delta(u_1 - |u + w/2|) \int du_2 \delta(u_2 - |u - w/2|)$  in the rate (3) and using the identity  $d(u + w/2) \wedge d(u - w/2) =$

$dw \wedge du$ , we arrive at the expected result

$$\begin{aligned} \Psi(T, p, u_1, u_2) &\equiv \frac{d\Gamma}{dT dp du_1 du_2} \\ &= \chi(T, p, u_1 + u_2) + \chi(T, p, -u_1 - u_2) \\ &\quad + \chi(T, p, u_1 - u_2) + \chi(T, p, -u_1 + u_2), \end{aligned} \quad (7)$$

expressing the differential rate in terms of variables accessible to degenerate parallax microlensing detection.

So far in this section we have ignored the question of the minimum amplification necessary for successful detection of a microlensing event. In particular, microlensing might produce sufficient magnification only in the Earth- (or satellite-) based detector, i.e., the magnification in the other detector (say ‘2’) could be too small for a reliable determination of  $\tau$  and  $u_2$ . To deal with this possibility, we will require  $u_1 < u_{\text{th}}$ ,  $u_2 < u_{\text{th}}$  for a detectable parallax (double, i.e. in both detectors) microlensing event, while single events will correspond to  $u_1 < u_{\text{th}}$ ,  $u_2 > u_{\text{th}}$  or  $u_1 > u_{\text{th}}$ ,  $u_2 < u_{\text{th}}$ , where  $u_{\text{th}}$  is a certain threshold value. The *detection* rate of events (both single and double) in one (say ‘1’) detector is thus

$$\begin{aligned} P(T, u_1) &\equiv \frac{d\Gamma^{(1)}}{dT du_1} \\ &= \int_0^\infty du_2 \int_{-\infty}^\infty dp \Psi(T, p, u_1, u_2) \\ &= \int_0^{u_{\text{th}}} du_2 \int_{-\infty}^\infty dp \Psi(T, p, u_1, u_2) + \Omega^{(1)}(T, u_1), \end{aligned} \quad (8)$$

where

$$\Omega^{(1)}(T, u_1) \equiv \frac{d\Gamma_{\text{single}}^{(1)}}{dT du_1} = \int_{u_{\text{th}}}^\infty du_2 \int_{-\infty}^\infty dp \Psi(T, p, u_1, u_2) \quad (9)$$

is the differential detection rate for single events, expressed in terms of the only available measurables,  $T$  and  $u_1$ . Of course,  $\Omega^{(1)}(T, u) = \Omega^{(2)}(T, u) = \Omega(T, u)$ . The differential rate  $P(T, u)$ , introduced in equation (8), is

$$\begin{aligned} P(T, u) &= 2Dr_{\text{E}}^4 \int d\mu \frac{dn_o}{d\mu} \left(\frac{\mu}{T^2}\right)^2 \int_0^1 dz H(z) [z(1-z)]^2 \\ &\quad \times \int_0^{2\pi} d\phi f_{\text{n}}(v_{\text{n}}, \phi). \end{aligned} \quad (10)$$

If we assume (as we will in the present paper) that the MHO mass function can be well approximated by a simple power law

$$\frac{dn_o}{d\mu} = \frac{1}{C_{\beta}(\alpha)} \frac{\mu^{\alpha}}{\mu_o^{\alpha+1}}, \quad (11)$$

where  $\beta = \log_{10}(\mu_{\text{max}}/\mu_{\text{min}})$ ,  $\mu_{\text{max}}$  and  $\mu_{\text{min}}$  are the upper and lower bounds of the mass range,  $\mu_o = \sqrt{\mu_{\text{max}}\mu_{\text{min}}}$  and

$$C_{\beta}(\alpha) = \begin{cases} \beta \ln 10 & \alpha = -1, \\ \frac{1}{\alpha+1} [10^{\beta(\alpha+1)/2} - 10^{-\beta(\alpha+1)/2}] & \alpha \neq -1, \end{cases} \quad (12)$$

the one-detector rate  $P(T, u)$  simplifies to

$$P(T, u) = 2Dr_{\text{E}}^4 \frac{T^{2(\alpha+1)}}{C_{\beta}(\alpha)\mu_o^{\alpha+1}} \int_{\mu_o \frac{10^{-\beta/2}}{T^2}}^{\mu_o \frac{10^{\beta/2}}{T^2}} y^{\alpha} F(y) dy, \quad (13)$$

where  $y \equiv \mu/T^2$  and

$$\begin{aligned} F(y) &= y^2 \int_0^1 dz [z(1-z)]^2 H(z) \\ &\quad \times \int_0^{2\pi} d\phi f_{\text{n}} \left[ r_{\text{E}} \sqrt{z(1-z)y}, \phi \right]. \end{aligned} \quad (14)$$

In the rest of the paper we will use a ‘composite’ notion of microlensing event including double (parallax) events and single events detected only in detector ‘1’ or ‘2’. The composite probability distribution function for degenerate parallax microlensing can then be obtained by introducing the normalising constant  $A$

$$\begin{aligned} \hat{\Psi}(T, p, u_1, u_2) &= \frac{1}{A} \Psi(T, p, u_1, u_2), \\ \hat{\Omega}(T, u) &= \frac{1}{A} \Omega(T, u), \end{aligned} \quad (15)$$

so that

$$\begin{aligned} \int_0^\infty dT \int_{-\infty}^\infty dp \int_0^{u_{\text{th}}} du_1 \int_0^{u_{\text{th}}} du_2 \hat{\Psi}(T, p, u_1, u_2) \\ + 2 \int_0^\infty dT \int_0^{u_{\text{th}}} du \hat{\Omega}(T, u) = 1. \end{aligned} \quad (16)$$

In order to take account of the detection condition  $u_1 < u_{\text{th}}$ ,  $u_2 < u_{\text{th}}$  in the case of *resolved* parallax microlensing detection, we multiply  $\chi(T, p, w)$  by the range of  $u$  (see Fig. 1) for which the double event detection condition is satisfied

$$\chi(T, p, w) \longrightarrow (2u_{\text{th}} - |w|)\chi(T, p, w), \quad (17)$$

( $|w| < 2u_{\text{th}}$ ), and thus obtain the differential *detection* rate of events characterised by the observables  $T, p$  and  $w$ . The relevant probability distribution for the detectable double events is then

$$\hat{\chi}(T, p, w) = \frac{1}{A} (2u_{\text{th}} - |w|)\chi(T, p, w), \quad (18)$$

where  $A$  has the same value as in the degenerate parallax case [one can show  $\int_0^{u_{\text{th}}} du_1 \int_0^{u_{\text{th}}} du_2 \Psi(T, p, u_1, u_2) = \int_{-2u_{\text{th}}}^{2u_{\text{th}}} dw (2u_{\text{th}} - |w|)\chi(T, p, w)$ ], thus yielding the normalisation

$$\begin{aligned} \int_0^\infty dT \int_{-\infty}^\infty dp \int_{-2u_{\text{th}}}^{2u_{\text{th}}} dw \hat{\chi}(T, p, w) \\ + 2 \int_0^\infty dT \int_0^{u_{\text{th}}} du \hat{\Omega}(T, u) = 1. \end{aligned} \quad (19)$$

### 3 MODELS OF MHO DISTRIBUTION AND KINEMATICS

In this paper we will consider a range of spherically symmetric models of the massive halo objects’ distribution and velocities. Probably the most commonly used model is the isothermal sphere with the velocity dispersion constant throughout the halo and the density profile which is well approximated by

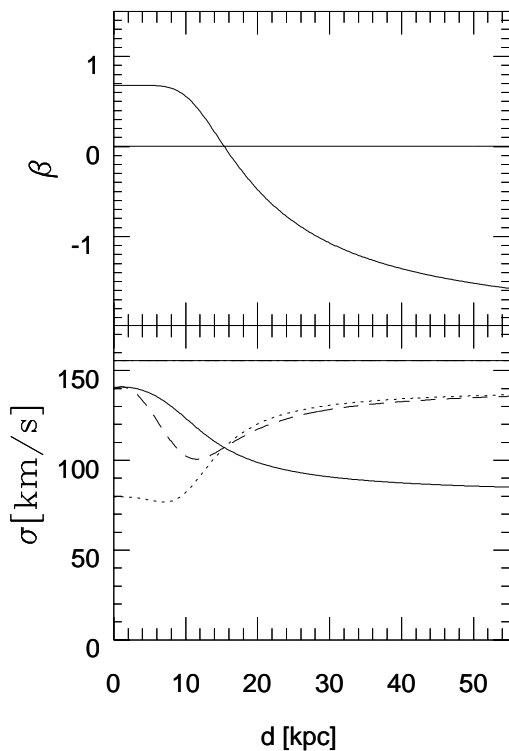


**Figure 3.** Anisotropy parameter  $\beta$  and velocity dispersion for the CS halo model as functions of the distance  $d$  from the Earth in the direction of LMC;  $\sigma_r$  is given by the solid line,  $\sigma_t = \sigma_j$  by the dotted line and  $\sigma_i$  [see paragraph following equation (24)] by the dashed line. The straight solid lines correspond to the singular isothermal sphere, SIS ( $\beta = 0$ ,  $\sigma = 156$  km/s) .

$$\rho(R) = \rho_o \frac{a^2 + R_\odot^2}{a^2 + R^2}, \quad (20)$$

where  $a \approx 5$  kpc is the ‘core’ radius and  $R_\odot = 8.5$  kpc is the distance of the Sun from the galactic centre. Assuming that the total (luminous + dark matter) halo density is distributed according to expression (20), one obtains the observed (approximately) flat rotation curve for the galaxy.

The MHO mass distribution, however, need not follow that of the total halo mass. We may, for instance, follow the hints provided by recent observations (Sommer-Larsen, Flynn & Christensen 1994, Sommer-Larsen *et al.* 1997) of the blue horizontal branch field stars (BHBFS) in the outer halo. These observations imply that the velocity dispersion changes from  $\beta \equiv 1 - \sigma_r^2/\sigma_t^2 > 0$  ( $\sigma_r$  and  $\sigma_t$  are velocity dispersions respectively in the radial and tangential direction relative to the Galactic centre) at smaller distances  $R$  from the centre of the Galaxy to  $\beta < 0$  at larger distances. The radial velocity dispersion is well described by the analytic fit

$$\sigma_r^2 = \sigma_o^2 + \sigma_+^2 \left[ \frac{1}{2} - \frac{1}{\pi} \tan^{-1} \left( \frac{R - r_o}{l} \right) \right], \quad (21)$$

where the best agreement with the observations is achieved with  $\sigma_o = 80$  km s<sup>-1</sup>,  $\sigma_+ = 145$  km s<sup>-1</sup>,  $r_o = 10.5$  kpc and  $l = 5.5$  kpc (these are the values used in paper I and the present one; more recent values, based on a larger sample of stars, are given in Sommer-Larsen *et al.* 1997). The BHBFS

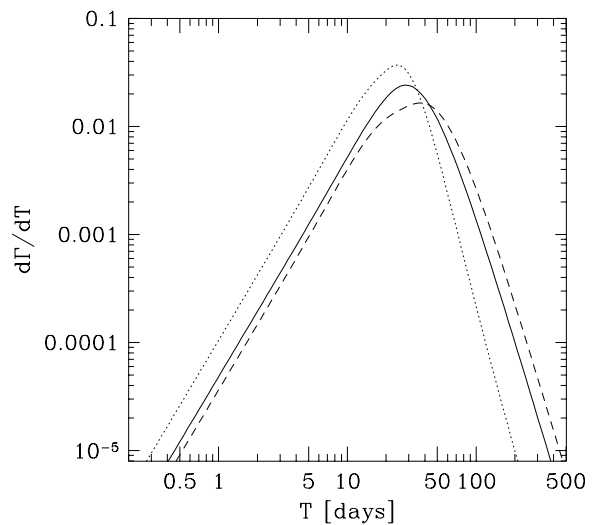


**Figure 4.** Differential rate  $d\Gamma/dT$  (normalised) for the SIS (solid line) and CS (short-dashed) halo models with Sun’s and LMC motion neglected. For the dotted line one assumes the CS model and takes into account the motion of the Sun and LMC. In all cases the mass function is a delta function centered on  $\mu = 0.4$ .

halo is close to spherical with the density that is well modeled by the power law  $\rho = \rho_o (R_\odot/R)^\gamma$ , where  $\gamma \approx 3.4$ .

The Jeans’ equation for spherical systems (Binney & Tremaine 1987) yields the tangential velocity dispersion

$$\sigma_t^2 = \frac{1}{2} V_c^2 - \left( \frac{\gamma}{2} - 1 \right) \sigma_r^2 + \frac{r}{2} \frac{d\sigma_r^2}{dR}, \quad (22)$$

where  $V_c = (-Rd\Phi/dR)^{1/2}$  is the (roughly constant) rotation velocity. This tangential dispersion is smaller than in the case of an isothermal sphere ( $\gamma = 2$ ,  $\sigma_r = \text{const.}$ ) with the same  $V_c$  (see Fig. 3).

We will, following paper I, model the velocity distribution by the Gaussian

$$f(v_r, v_\theta, v_\phi) = \frac{1}{(2\pi)^{3/2}} \frac{1}{\sigma_r \sigma_t^2} \exp \left[ -\frac{1}{2} \left( \frac{v_r^2}{\sigma_r^2} + \frac{v_\theta^2 + v_\phi^2}{\sigma_t^2} \right) \right], \quad (23)$$

where  $\sigma_r$  and  $\sigma_t$  are given by equations (21) and (22) for power-law density profiles. The relevant distribution [used, e.g., in the rate (3)] of velocities orthogonal to the line of sight is then

$$f(v_n, \phi) = \frac{1}{2\pi \sigma_i \sigma_j} \exp \left[ -\frac{1}{2} \left( \frac{[v_n \cos(\phi + \phi_o) + s_i]^2}{\sigma_i^2} + \frac{[v_n \sin(\phi + \phi_o) + s_j]^2}{\sigma_j^2} \right) \right]. \quad (24)$$

For the above equation we have introduced orthonormal vectors in the plane orthogonal to the line of sight:  $\hat{i}$  is in the plane determined by the Sun, LMC and the Galactic centre (GC) and points in the general direction of GC;  $\hat{j} = \mathbf{k} \times \hat{i}$ , where  $\mathbf{k}$  points along the Sun-LMC line of sight. Thus,  $s_i$  and  $s_j$  are the corresponding components of the local ( $z$ -dependent) velocity of the line of sight relative to

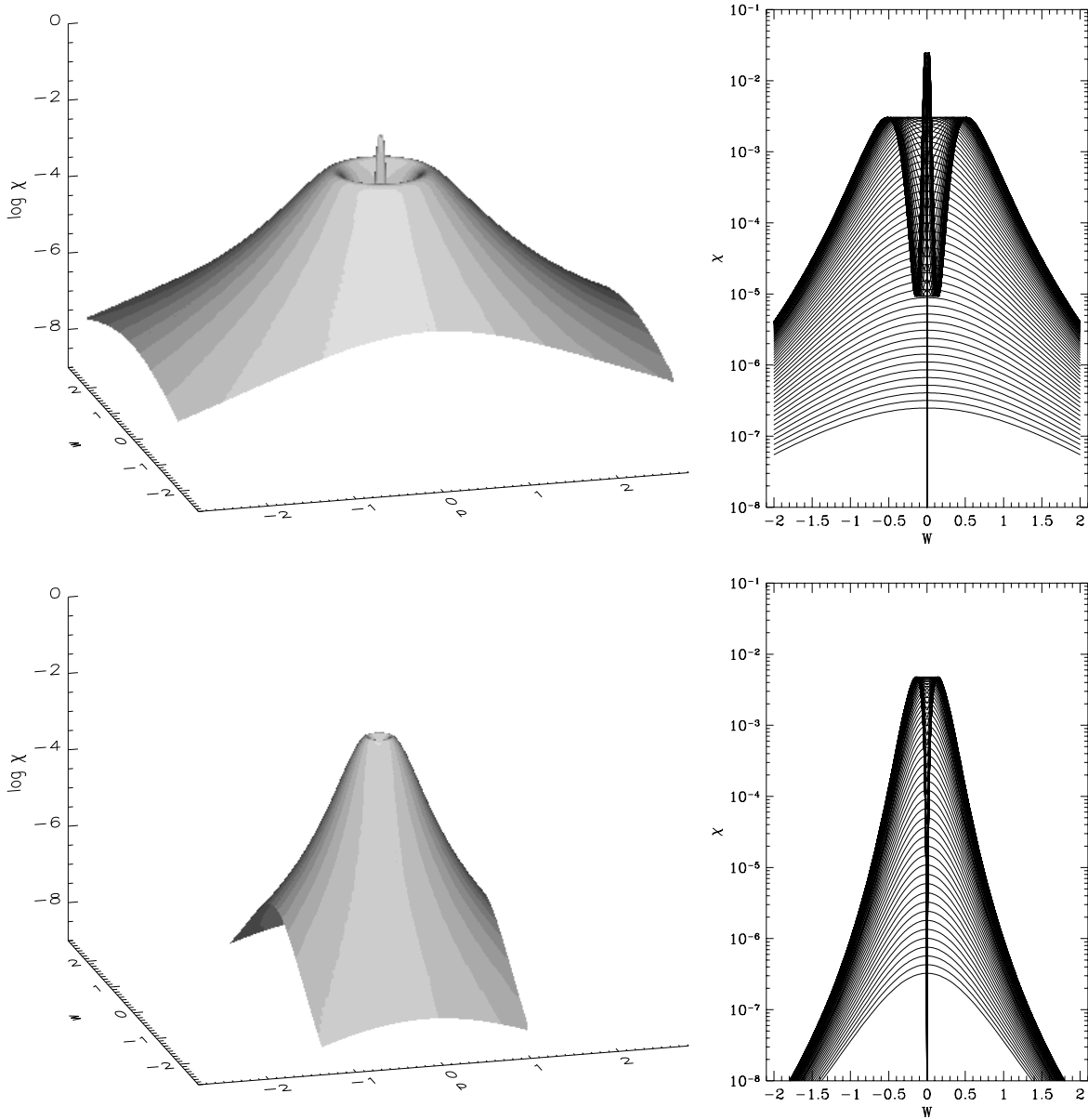


**Figure 5.** Plots of  $\chi$  with the SIS halo (Sun's and LMC motion neglected) and a delta mass function ( $\mu = 0.4$ ) at  $T = 14.2$  (top) and  $T = 84.7$  (bottom) days.

the galaxy,  $\phi_o$  is the angle between the '1'-'2' axis and  $\hat{i}$ ,  $\sigma_j = \sigma_t$  and  $\sigma_r^2 = \cos^2 \delta \sigma_t^2 + \sin^2 \delta \sigma_r^2$  [ $\sin \delta = (R_\odot/R) \sin \iota$  and  $R^2 = R_\odot^2 + (zD)^2 - 2zDR_\odot \cos \iota$  ( $\iota = 82^\circ$  is the angle between GC and LMC as observed from the Earth)]. Detailed derivations and numerical values are given in the Appendix.

As in paper I, the halo model corresponding to BHBFS with the power-law density profile  $\gamma = 3.4$  and the dispersion given by (21) and Jeans' equation will be called the 'concentrated sphere' ('CS'). More generally, we will assume for our study that the MHO halo can be described by a member of a class of models specified by five parameters:  $\gamma$ ,  $\sigma_o$ ,  $\sigma_+ r_o$  and  $l$ . For instance, the model with  $\gamma = 2$  and constant velocity dispersion  $\sigma_r = \sigma_t = V_c/\sqrt{2} = 156$  km/s (i.e.,

$\sigma_o = V_c/\sqrt{2}$ ,  $\sigma_+ = 0$ ) is just the familiar singular isothermal sphere (SIS).

#### 4 DISTRIBUTION OF MEASURABLE QUANTITIES

In order to understand basic features of the distribution functions  $\chi(T, p, w)$  [and consequently  $\Psi(T, p, u_1, u_2)$ ] and  $\Omega(T, u)$  we will at first limit ourselves to the relatively simple case of the SIS halo, neglect the motion of the Sun (i.e., the detectors) and the LMC and assume that all MHOs have the same mass,  $\mu = \bar{\mu}$  (see Fig. 4).

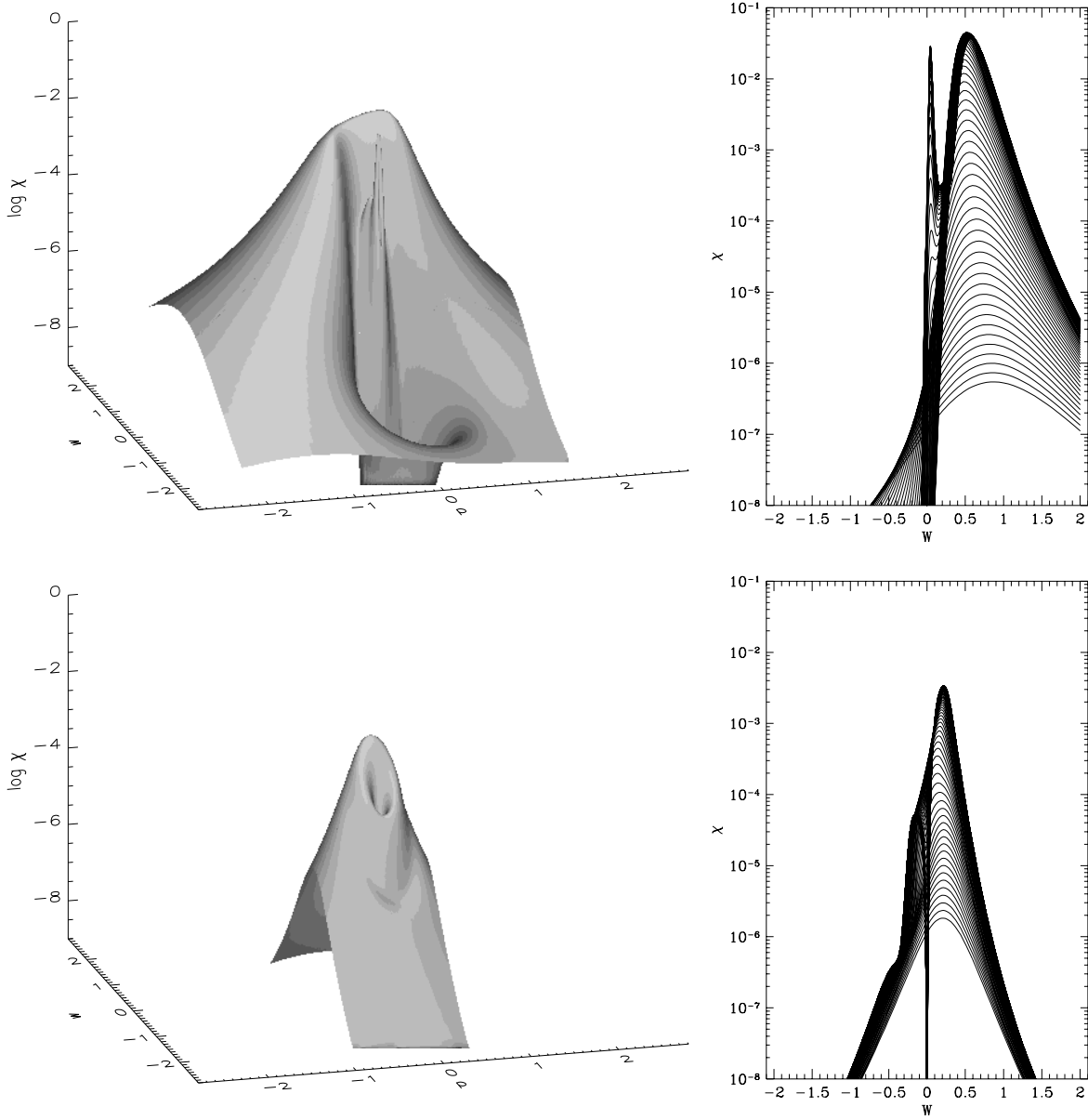


**Figure 6.** Plots of  $\chi$  with the CS halo (Sun's and LMC motion taken into account) and a delta mass function ( $\mu = 0.4$ ) at  $T = 15.1$  (top) and  $T = 81.4$  (bottom) days.

With the above assumptions

$$\chi(T, p, w) \propto \frac{(1-z)^2 z^4 H(z)}{T^4} \exp\left[-\frac{1}{2} \frac{r_E^2 \mu}{\sigma^2} \frac{z(1-z)}{T^2}\right], \quad (25)$$

where  $z(p, w)$  is given by equation (4). At sufficiently small  $a^2 = p^2 + w^2$ , a MHO is near LMC,  $z \approx 1$ ,  $1-z \approx (r_E/r)^2 \mu a^2$  and we thus have

$$\chi \sim a^4 \exp\left[-\frac{1}{2} \left(\frac{r_E^2 \mu}{r \sigma T}\right)^2 a^2\right]. \quad (26)$$

Near the origin of the  $p, w$  plane  $\chi$  grows at first as  $a^4$  (from  $\chi = 0$  at  $a = 0$ ) to a maximum value at  $a_1 = 2r\sigma T/r_E^2 \mu$  (see the 'funnel' emerging from  $w = 0$  on the right of Fig. 5,

which is a projection along the  $p$ -axis of the 3D plot on the left), which for the values of this SIS model parameters and  $\mu = 0.4$ ,  $r = 2$  AU takes on value  $a_1 = T/508$  d.

At large  $a$ ,  $z \approx (r/r_E)^2/\mu a^2$  (close to the detector at  $z = 0$ ) and thus

$$\chi \sim \frac{1}{a^8} \exp\left[-\frac{1}{2} \left(\frac{r}{\sigma T}\right)^2 \frac{1}{a^2}\right]. \quad (27)$$

This expression reaches a maximum at  $a_2 = (1/2^{3/2})r/\sigma T = 7.9$  d/ $T$ , and falls off as  $\chi \propto a^{-8}$  for  $a > a_2$ .

For  $T < T_o$ , where

$$T_o \equiv \frac{1}{2^{5/4}} \frac{r_E \sqrt{\mu}}{\sigma} = 63 \text{ d}, \quad (28)$$

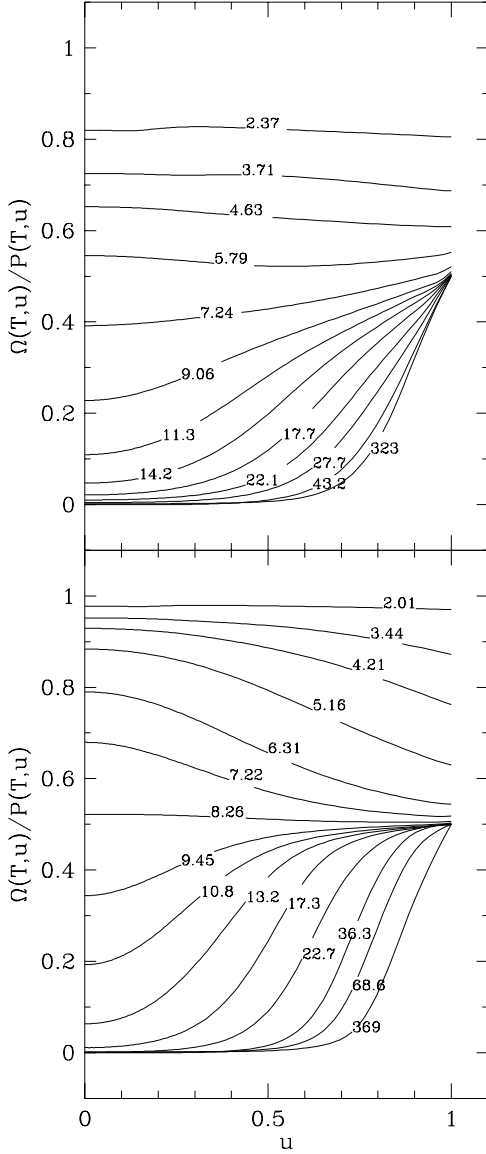


**Figure 7.** The fraction  $\Omega(T, u)/P(T, u)$  of events detected in one detector (i.e., with  $u < u_{\text{th}} = 1$ ) that are *not* detected in the other detector. The upper panel gives the plots for the SIS halo model (without Sun’s or LMC motion) and the bottom for the CS (with Sun’s and LMC motion) model, both with a delta mass function,  $\mu = 0.4$ . The lines are labeled with event durations  $T$  in days. The total (i.e., integrated over  $T$ ) fraction of *single* events out of all events detected in a detector is 12% in the upper case and 20% in the bottom case: the CS model gives more events at low  $z$ , where  $R_E/r(1-z)$  is smaller.

we have  $a_1 < a_2$  and an annular ‘valley’ will exist between the two maxima (see the top of Fig. 5) separating the inner ‘funnel’ from the outer circular wall of the ‘volcano.’ The detected events would thus belong to two distinct classes distinguished by the magnitude of  $a$ .

As we shift toward larger  $T$ ’s the ‘valley’ turns shallower and flattens out completely around  $T = T_o$ . For  $T > T_o$  (see

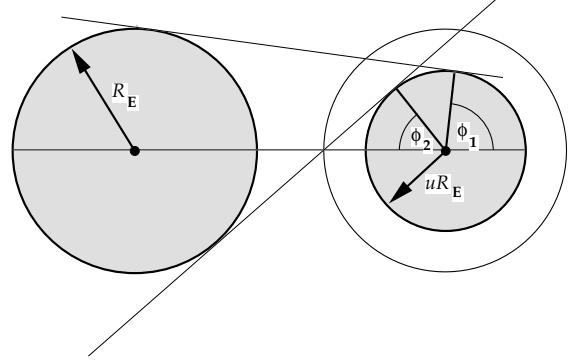


**Figure 8.** The lines tangential to both the circles of radius  $R_E$  and  $uR_E$  are drawn to find the sector of size  $2(\phi_1 + \phi_2)$  from which the events at  $u (< u_{\text{th}} = 1)$  in the right-hand side detector are not detectable by the one on the left-hand side. The distance between the centres of the circles is  $r(1-z)$ .

the bottom of Fig. 5) only one maximum at  $a = a_1$  will persist.

Introduction of the anisotropic velocity dispersion of the CS halo model will distort the circular contour lines of Fig. 5 into elliptical ones. In addition, switching on the motion of the Sun and LMC (Earth’s revolution around the Sun neglected; the Earth-satellite line lies in the ecliptic and chosen orthogonal to the line of sight; see the Appendix) will ‘erode’ the outer wall of the ‘volcano’ asymmetrically (Fig. 6): more MHOs will cross the 1-2 line of Fig. 1 in the upward direction. The motion of the line of sight through the rest frame of the halo will also lead to a general shift of the differential event rate  $d\Gamma/dT$  toward shorter durations (Fig. 4).

In Fig. 7 we plot for various durations  $T$  the fraction  $\Omega(T, u)/P(T, u)$  of events detected in one detector (say,  $u \equiv u_2 < u_{\text{th}}$ ) that are not detectable ( $u_1 > u_{\text{th}}$ ) in the other one. At short  $T$ ’s (few days) the event rate is dominated by MHOs that cross the line of sight close to the Sun. For these MHOs  $R_E = r_E \sqrt{\mu} \sqrt{z(1-z)}$  is smaller than the projected separation  $r(1-z)$  between the lines of sight with respect to the two detectors ( $a > 1$ ). The elementary construction of Fig. 8 shows that of all MHOs passing at impact parameter  $uR_E$  relative to detector 2, the fraction

$$\begin{aligned} \frac{\Omega(T, u)}{P(T, u)} &\approx \frac{\phi_1 + \phi_2}{\pi} \\ &= \frac{1}{\pi} \left[ \cos^{-1} \frac{R_E}{r(1-z)}(1-u) + \cos^{-1} \frac{R_E}{r(1-z)}(1+u) \right] \\ &\approx 1 - \frac{2}{\pi} \frac{R_E}{r(1-z)} - \frac{1}{3\pi} \left[ \frac{R_E}{r(1-z)} \right]^3 (1+3u^2) \end{aligned} \quad (29)$$

will pass at impact parameters greater than  $R_E$  with respect to detector 1 and thus not be detected if  $u_{\text{th}} = 1$  (we here assume the 2-dimensional velocity distribution is isotropic as is the case for the SIS model without the Sun’s and LMC’s motion).

At  $R_E \ll r(1-z)$  [ $z < 1/(1 + \mu r_E^2/r^2) \approx (r/r_E)^2/\mu = 0.02$ ] fractioning (29) depends weakly on  $u$ ; the flatness of the corresponding curves can be observed in the top part of



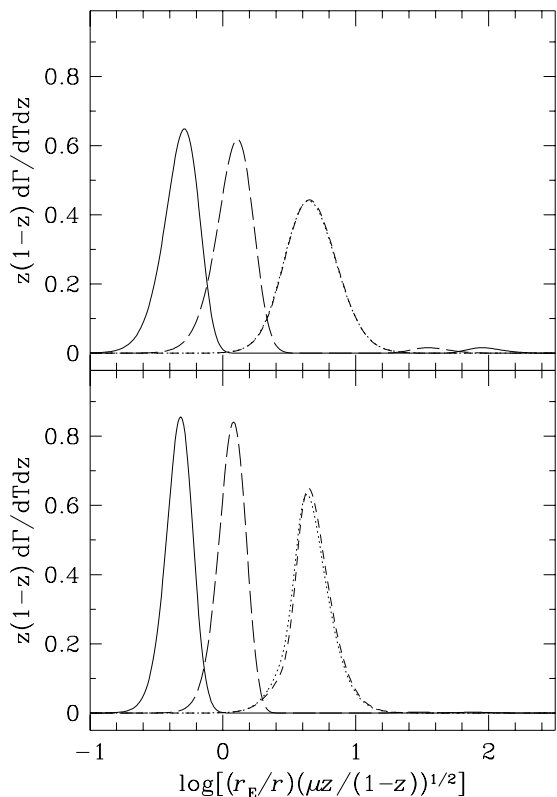


**Figure 9.** Normalised (i.e. of a constant area under the curve)  $d\Gamma/dTdz$  at  $T = 4.6$  (solid),  $T = 11.2$  (long dash),  $T = 166$  (dotted) and  $T = 361$  days (short dash) for the SIS (without Sun’s or LMC motion; top) and CS (with Sun’s and LMC motion; bottom) halo models. In both cases the mass function is delta at  $\mu = 0.4$ . The 166d and 361d curves are virtually indistinguishable.

Fig. 7. Naturally, the  $\Omega/P$  curves are depressed as  $T$  [and thus  $R_E/r(1-z)$ ] is increased.

For MHOs passing at larger  $z > 0.02$  (corresponding to typical times  $T \approx R_E/\sqrt{2}\sigma > r/\sqrt{2}\sigma \approx 15$  d) the Einstein radius will be longer than the projected Earth-satellite distance  $r(1-z)$ . This means that an event of a small impact parameter  $u < 1 - r(1-z)/R_E$ , with respect to one detector, will inevitably be detected [ $\Omega(T, u)/P(T, u) = 0$ ] by the other one. For  $u > 1 - r(1-z)/R_E$ , the fraction detectable in only one detector rises approximately as

$$\frac{\Omega(T, u)}{P(T, u)} = \frac{1}{\pi} \cos^{-1} \frac{R_E}{r(1-z)} (1-u) \quad (30)$$

with increasing  $u$  and reaches  $1/2$  at  $u = u_{\text{th}} = 1$ .

The correspondence between the event durations and typical  $z$ ’s is illustrated in Fig. 9. The differential rate  $d\Gamma/dTdz$  is relatively sharply peaked if plotted with respect to the coordinate  $(r_E/r)[\mu z/(1-z)]^{1/2} = R_E/r(1-z) = 1/a$  instead of  $z$  [the area element below a curve in Fig. 9 differs from  $(d\Gamma/dTdz)dz$  only by a constant factor]; we used this fact in the above discussion to relate a narrow range of  $z$  (or, rather, simply a *single* value of  $z$ ) to each  $T$ .

## 5 INFERENCE OF THE MHO MASS FUNCTION AND THE HALO STRUCTURE

Even at first sight it seems obvious that the increased amount of information obtained from parallax microlensing measurements should allow a more reliable determination of the structure of the halo and the MHO mass function than just the measurements of event durations. Indeed, the measurable quantity  $pT = r(1-z) \cos \phi/v_n$  (equation 2) involves only the *kinematic* properties of a MHO (i.e., excluding its mass). In the case of resolved parallaxes, an additional quantity,  $w$ , is measured and this gives us the 2-dimensional velocity projected on the observer’s plane (the so-called *reduced* velocity; see. e.g., Gould 1994b)

$$\tilde{\mathbf{v}} \equiv \frac{1}{1-z} \mathbf{v}_n = \frac{r}{T} \frac{\mathbf{a}}{a^2} = \frac{r}{T} \frac{1}{p^2 + w^2} (p, w). \quad (31)$$

Although the 4-fold ambiguity of the degenerate parallaxes reduces the quality of available information, both types of parallax microlensing would constrain the halo independently of the MHO masses; this should make it possible to separate the effects of the masses and determine the MHO mass function.

In order to assess the information gain due to parallax microlensing we will investigate simulated maximum likelihood inference of the five parameters ( $c_1 \equiv \gamma$ ,  $c_2 \equiv \sigma_o$ ,  $c_3 \equiv \sigma_+$ ,  $c_4 \equiv r_o$ ,  $c_5 \equiv l$ ) of the halo model and the three parameters ( $c_6 \equiv \bar{\mu}$ ,  $c_7 \equiv \alpha$ ,  $c_8 \equiv \beta$ ) of the mass function based on the normalised probability distributions  $\hat{\chi}(T, p, w)$ ,  $\hat{\Omega}(T, u)$  (equation 19) for resolved or  $\hat{\Psi}(T, p, u_1, u_2)$ ,  $\hat{\Omega}(T, u)$  (equation 16) for degenerate parallax measurables.

Ideally, one would prefer to obtain an answer through a series of Monte-Carlo simulations, but the enormous numerical task of computing the above 3-dimensional distribution  $\chi$  for many points in the 8-dimensional parameter space compels us to seek more economical alternatives. For a sufficiently large number  $N$  of detected events, the average errors  $\sigma_\mu \equiv \langle [c_\mu - c_\mu^{(o)}]^2 \rangle^{1/2}$  of the parameters ( $c_\mu^{(o)}$  is the ‘real’ value of a parameter) can be shown (see, e.g., paper I) to approach asymptotically the Cramer limit

$$\langle (c_\mu - c_\mu^{(o)}) (c_\nu - c_\nu^{(o)}) \rangle \rightarrow \mathcal{C}_{\mu\nu}, \quad (32)$$

where  $\mathcal{C}_{\mu\nu}$  is the inverse of the information matrix

$$I_{\mu\nu}^{(N)} = N \int \int \int \int dT dP du_1 du_2 \frac{\hat{\Psi}_{,\mu} \hat{\Psi}_{,\nu}}{\hat{\Psi}} + 2N \int \int dT du \frac{\hat{\Omega}_{,\mu} \hat{\Omega}_{,\nu}}{\hat{\Omega}} \quad (33)$$

( $_{,\mu}$  denotes derivative with respect to the  $\mu$ ’th parameter) for degenerate parallaxes and by analogy for the resolved parallaxes.

In our numerical experiment we assume that the parameters of the concentrated sphere (CS) describe accurately the MHO halo. The Cramer errors of the inference of the mass-function parameters for  $N = 100$  are shown in Fig. 10 as functions of the mass-function slope  $\alpha$ . The resolved parallax errors obtained with the assumption that both the halo structure and the mass function parameters were unknown (and thus variable in the maximum likelihood fitting) are given as solid lines. For comparison, we also show the Cramer-limit errors (dotted lines) for measurements of

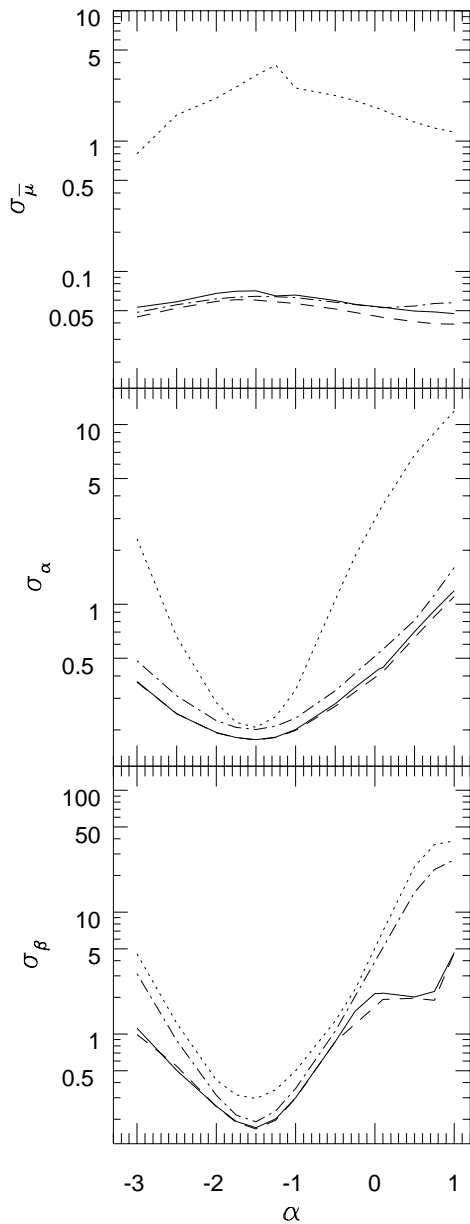


**Figure 10.** The Cramer-limit errors with an unknown (variable) halo from resolved parallaxes (solid lines) and event durations only (dotted). For a fixed CS halo model, the errors are shown as dashed lines (resolved parallaxes) and dot-dashed (event durations only) lines. All errors are given for  $\bar{\mu} = 0.4$ ,  $\beta = 2$  and  $N = 100$  events.

event durations only. In addition, we plot the resolved parallax errors (dashed lines) and the errors based on event durations only (dot-dash) assuming that the halo parameters are known precisely (and thus not varied for the maximum likelihood fit). In all computations we take into account the motion of the Sun and LMC, assume  $r = 2$  and that the Earth-satellite segment is in the ecliptic and orthogonal to the Earth-LMC line of sight (see the Appendix).

The most striking feature of these plots is a significant reduction of the error in  $\bar{\mu}$  brought about by parallax measurements. As shown in paper I, by changing the parameters

of the halo model one can match closely event duration distribution curves corresponding to widely different average masses. This is reflected in the large errors in  $\bar{\mu}$  if the halo parameters are allowed to vary in addition to the parameters of the mass function. The extra information provided by parallaxes effectively allows us to constrain the halo as to bring  $\sigma_{\bar{\mu}}$  down to the values comparable to those of inference with a fixed (i.e., ‘known’) halo model. (Notice that the gain in accuracy due to parallaxes for a known halo structure is modest by comparison.)

In paper I we have concluded that for a certain range of  $\alpha$  (very roughly,  $-2 \lesssim \alpha \lesssim 0$ ) the inference of  $\alpha$  and  $\beta$  is relatively weakly affected by the uncertainty of the halo structure. This again is manifested in errors of the same (small) order near  $\alpha = -1.5$  in all four cases shown in Fig. 10. However, away from  $\alpha = -1.5$ ,  $\sigma_{\alpha}$  and  $\sigma_{\beta}$  grow large for event duration-based inference. Here again, the parallaxes restrain this growth significantly (especially for  $\sigma_{\alpha}$ ) and keep the errors down in the range characteristic of the fixed-halo inference. Interestingly, degenerate parallax errors  $\sigma_{\bar{\mu}}$ ,  $\sigma_{\alpha}$  and  $\sigma_{\beta}$  are only a few percent smaller than the resolved parallax values (and we omit the corresponding plots).

As suggested above, the significant improvement in the accuracy of the mass function determination should be ascribed to the disentanglement of the halo structure from the MHO masses. This disentanglement is obvious from the plots in Fig. 11 of the correlation matrix

$$\frac{C_{\mu\nu}}{\sqrt{C_{\mu\mu}}\sqrt{C_{\nu\nu}}}. \quad (34)$$

The off-diagonal spikes ‘coupling’ the halo with the mass function are noticeably less pronounced in the parallax case (right). [Notice, e.g., the strong correlation between  $\bar{\mu}$  and  $\gamma$  in the duration based inference (left) and its significant drop in the parallax case (right).]

Further comparison of the two plots of Fig. 11 also shows a significant reduction in the correlation among some of the halo parameters due to the parallax measurements. Does this imply that the halo structure itself could be inferable? Figure 12 indeed displays a remarkable suppression of the Cramer errors of the halo parameters’ inference: the (resolved) parallax errors at least are of the same order of magnitude as the parameters themselves or smaller.<sup>†</sup> In particular, the density profile index  $\gamma$  can be determined rather accurately. [The difference between the degenerate and resolved parallax errors is more pronounced for the halo model parameters than for the mass function; still, the degenerate parallax errors are larger than the resolved parallax ones by at most 20%. The measurement of  $p$  and the information contained in  $u_1$ ,  $u_2$  and  $\Omega(T, u)$  are thus sufficient to constrain the halo even if the determination of  $w$  is subject to the 4-fold ambiguity.]

<sup>†</sup> As discussed in paper I, the Cramer errors can serve as reliable estimates of actual errors only if they are small in comparison with the corresponding parameters that one is trying to infer. Typically, we would expect the nonlinear dependence of the distribution function of the observables on the underlying parameters to make the actual errors smaller than the Cramer estimates when these are relatively large. In this case the actual errors would fall slower than  $N^{-1/2}$  and approach the Cramer limit from below.

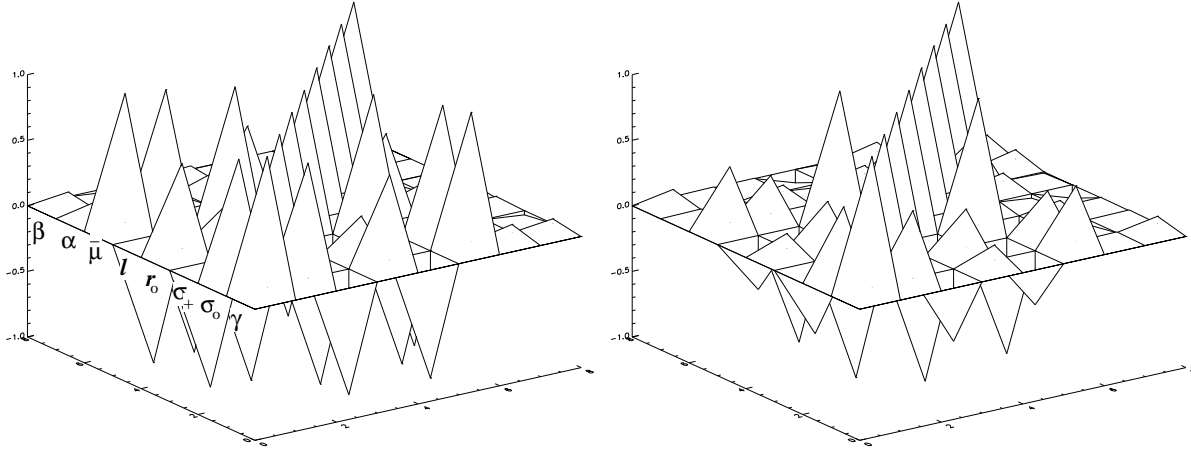


**Figure 11.** Correlation matrices for Cramer errors of inference based on event durations only (left) and resolved parallaxes (right). The underlying halo model is CS and the parameters of the mass function function are  $\bar{\mu} = 0.4$ ,  $\alpha = -1.5$  and  $\beta = 2$ .

$\sigma_{(1)} = 0.033$ ,	$\mathbf{V}_{(1)} =$	( 0.7667, 0.2005, 0.5791, 0.1562, -0.1037, 0.0233, 0.0149, -0.0258 )
$\sigma_{(2)} = 0.795$ ,	$\mathbf{V}_{(2)} =$	( 0.0362, 0.7289, -0.0838, -0.5037, 0.4541, 0.0229, -0.0048, 0.0035 )
$\sigma_{(3)} = 0.126$ ,	$\mathbf{V}_{(3)} =$	( -0.4744, 0.2243, 0.4946, 0.1677, -0.0685, 0.3439, -0.5733, 0.0175 )
$\sigma_{(4)} = 0.383$ ,	$\mathbf{V}_{(4)} =$	( 0.0511, 0.2676, -0.3075, 0.8129, 0.4111, 0.0083, -0.0103, -0.0338 )
$\sigma_{(5)} = 3.316$ ,	$\mathbf{V}_{(5)} =$	( -0.0158, -0.5050, 0.3601, -0.0903, 0.7789, -0.0143, -0.0019, -0.0001 )
$\sigma_{(6)} = 0.182$ ,	$\mathbf{V}_{(6)} =$	( 0.3327, -0.1966, -0.3563, -0.1221, 0.0442, 0.8117, -0.2121, 0.0540 )
$\sigma_{(7)} = 0.102$ ,	$\mathbf{V}_{(7)} =$	( -0.2675, 0.1085, 0.2431, 0.0859, -0.0271, 0.4702, 0.7796, -0.1434 )
$\sigma_{(8)} = 0.081$ ,	$\mathbf{V}_{(8)} =$	( -0.0270, 0.0343, 0.0510, 0.0499, 0.0048, 0.0186, 0.1351, 0.9871 )

**Table 1.** Eigen-errors (for  $N = 100$  events) and the corresponding eigen-vectors of the relative error matrix for the CS halo and  $\bar{\mu} = 0.4$ ,  $\alpha = -1.5$  and  $\beta = 2$ .

The residual but still considerable correlations among the errors of the halo parameters indicate that some combinations (functions) of them (together with the mass function parameters) may be possible to determine with a significantly higher accuracy. In order to investigate this possibility we examine the eigen-values and eigen-vectors of the *relative* error matrix

$$\Delta_{\mu\nu} \equiv \frac{C_{\mu\nu}}{c_{\mu}^{(o)} c_{\nu}^{(o)}} = \left\langle \left( \frac{c_{\mu}}{c_{\mu}^{(o)}} - 1 \right) \left( \frac{c_{\nu}}{c_{\nu}^{(o)}} - 1 \right) \right\rangle, \quad (35)$$

i.e., those normalised vectors  $\mathbf{V}_{(\rho)}$  ( $V_{(\rho)}^{\mu} V_{(\rho)}^{\mu} = 1$ , using Einstein's convention for summation over the repeated index  $\mu$ ) that satisfy the eigen-equation

$$\Delta_{\mu\nu} V_{(\rho)}^{\nu} = \sigma_{(\rho)}^2 V_{(\rho)}^{\mu}. \quad (36)$$

These eigenvectors correspond to the linear expansions of the desired functions of the parameters in the vicinity of  $c_{\mu}^{(o)}$ ; they indicate the mutually independent (uncorrelated) infinitesimal displacements in the parameter space caused by statistical errors of parallax microlensing detections. In a certain sense, they are the *eigen-modes* of the halo model (plus the mass function) as viewed through the 'instrument' of parallax microlensing.

We illustrate the above point by a specific example. Table 1 contains the square roots ('eigen-errors') of the eigen-values along with the eigen-vectors of the relative error matrix, assuming again the CS halo model and  $\bar{\mu} = 0.4$ ,  $\alpha = -1.5$  and  $\beta = 2$  (same as for Fig. 11). We immediately notice that the eigen-errors for the eigen-'modes' are small ( $\sigma_{(\rho)} < 1$ ) except for a single mode ( $\sigma_{(5)} = 3.316$ ). This, the 5'th mode 'mixes' rather strongly  $c_2 = \sigma_o$ ,  $c_5 = l$  and to a lesser degree  $c_3 = \sigma_+$  (see the corresponding components of  $\mathbf{V}_{(5)}$ ). Its mass function components,  $V_{(5)}^6$ ,  $V_{(5)}^7$  and  $V_{(5)}^8$ , are very small which explains why its large associated eigen-error does not lead to large errors of the mass function parameters. On the other hand, although there is an eigen-vector,  $\mathbf{V}_{(3)}$ , that strongly mixes the halo and the mass mass function parameters, its relatively small eigen error,  $\sigma_{(3)} = 0.126$  contributes little to the errors of the mass function parameters and thus gives at most moderate correlations between these and the halo-model errors.

In Fig. 13 we compare changes in the halo model caused by a displacement in the direction of the vector  $V_{(1)}$  of a small eigen-error with a displacement along  $V_{(5)}$ . Notice that a much larger displacement ( $\epsilon = 0.5$ ) is needed along  $V_{(5)}$  to cause a discernible effect. In addition, these changes

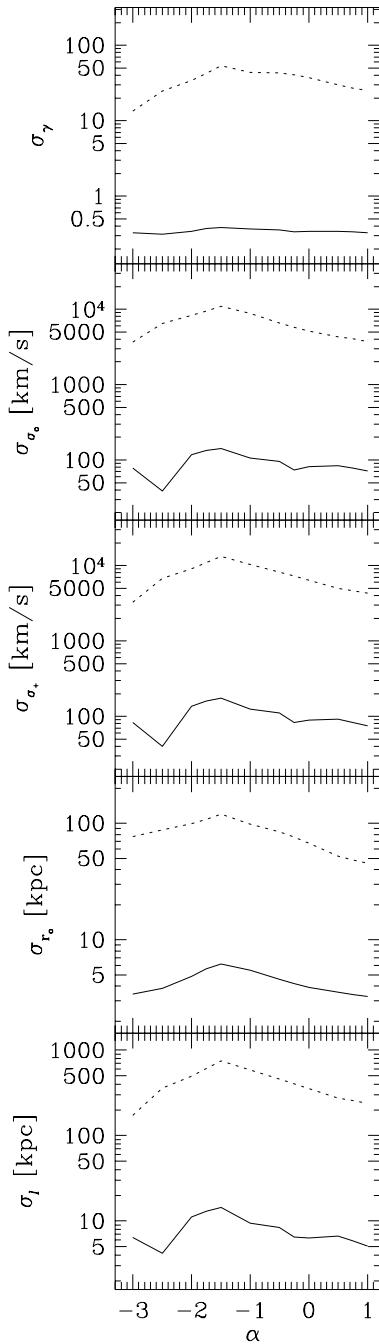


**Figure 12.** The Cramer-limit errors (at  $\bar{\mu} = 0.4$ ,  $\beta = 2$  and  $N = 100$ ) of the halo-model parameters from resolved parallaxes (solid lines) and event durations only (dotted lines).

tend to be concentrated at larger distances, where the event rate (recall  $\gamma = 3.4$ ) is smaller; microlensing is, not surprisingly, relatively insensitive to such displacements along  $V_{(5)}$  in the parameter space. As a consequence, the large associated eigen-error,  $\sigma_{(5)}$ , is the leading culprit for the relatively large errors of  $c_2 = \sigma_o$ ,  $c_5 = l$  and  $c_3 = \sigma_+$  evident in Fig. 12. By contrast, parallax microlensing constrains fairly well the displacements along the other directions. In particular, the

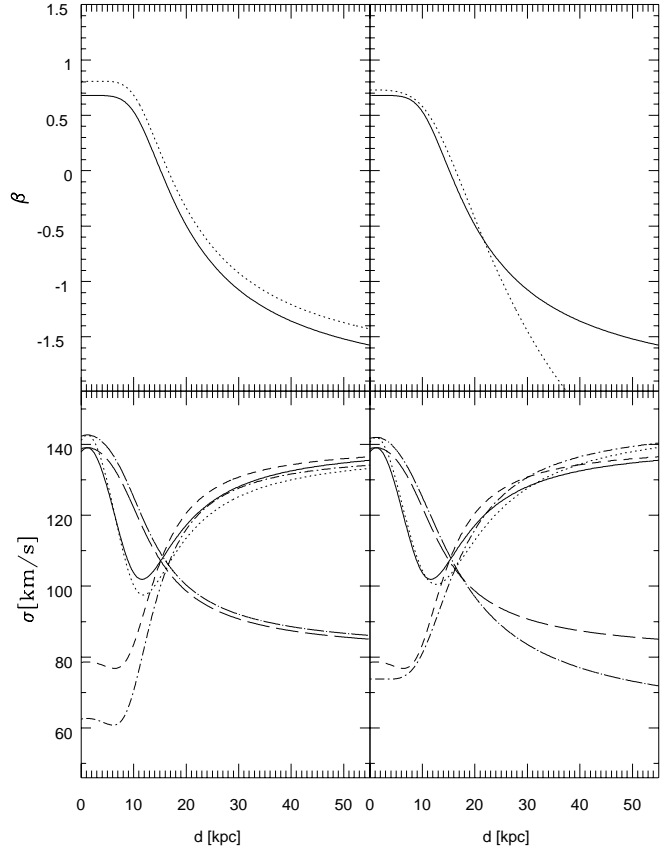


**Figure 13.** Comparison of the lowest-error halo mode,  $\mathbf{V}_{(1)}$ , at  $\epsilon = 0.05$  (left) and the highest-error,  $\mathbf{V}_{(5)}$  at  $\epsilon = 0.5$  (right) halo mode. In the bottom plots  $\sigma_r$  of the CS model is given as long dashed lines while its ‘shifts’ corresponding to  $\epsilon\mathbf{V}_{(1)}$  or  $\epsilon\mathbf{V}_{(5)}$  are given as dot-long dashed lines. The  $\sigma_j = \sigma_r$  lines are short dashed (CS) and dot-short dashed (shifted from CS). The  $\sigma_i$  lines are solid (CS) and dotted (shifted). In all cases  $\bar{\mu} = 0.4$ ,  $\alpha = -1.5$  and  $\beta = 2$ .

eigen-modes *closest* to the parameters of the mass function ( $V_{(6)}$ ,  $V_{(7)}$  and  $V_{(8)}$ ) all have rather small eigen-errors.

The coefficient  $\epsilon = 0.5$  used in Fig. 13 for the displacement along  $V_{(5)}$  is considerably smaller than the associated eigen-error  $\sigma_{(5)} = 3.3$  (see Table 1); the relatively small  $\epsilon$  allows us to stay near the ‘linear’ range of shifts in the structure of the halo (the range of the validity of the Cramer errors). At  $\epsilon = 3.3$  the structure would be changed radically, far beyond what one might expect on the basis of small linear displacements. This likely implies that actual errors would be smaller than the Cramer-limit estimate. The results of such strongly *non-linear* shifts can be studied only by means of Monte-carlo simulations which are beyond the scope of this paper.

The CS halo discussed so far can be regarded as a typical member of our class of spherical models. On the other hand, SIS is peculiar in that the parameters  $r_o$  and  $l$  can be arbitrary as long as  $\sigma_+ = 0$ . Might this ‘degeneracy’ lead to a large uncertainty in the inference of the halo structure?

To explore this issue we assume  $\gamma = 2$ ,  $\sigma_o = 156$  km  $\sigma_+ = 10$  km,  $r_o = 10.5$  kpc and  $l = 5.5$  kpc, only slightly deviating from SIS. The root-quadratic dependence of  $\sigma_r$

	$\sigma_{(3)}\mathbf{V}_{(3)}$	$\sigma_{(4)}\mathbf{V}_{(4)}$	$\sigma_{(5)}\mathbf{V}_{(5)}$
$\gamma$	2.02	1.81	1.77
$\sigma_o$ [km/s]	170	116	15
$\sigma_+$ [km/s]	81	111	272
$r_o$ [kpc]	$-1.7 \times 10^3$	$-1.1 \times 10^3$	$-2.5 \times 10^3$
$l$ [kpc]	$-0.6 \times 10^3$	$-0.5 \times 10^3$	$4.3 \times 10^3$
$\sigma_r$ [km/s]	186	122	158
$\sigma_t$ [km/s]	155	160	164

**Table 2.** Halo structure parameters and radial and tangential velocity dispersions after displacements  $\sigma_{(i)}\mathbf{V}_{(i)}$  in the parameter space.

on  $\sigma_o$  and  $\sigma_+$  (equation 21) suggests we use the squares  $c_2 = \sigma_o^2 = 2.4 \times 10^4 \text{ km}^2/\text{s}^2$  and  $c_3 = \sigma_+^2 = 100 \text{ km}^2/\text{s}^2$  among the parameters whose inference we estimate in the Cramer limit.

At  $N = 100$  events (we take  $\bar{\mu} = 0.4$ ,  $\alpha = -2$  and  $\beta = 2$ ) the resolved parallax errors for the density profile,  $\sigma_1 = 0.36$ , and the mass-function parameters,  $\sigma_6 = 0.08$ ,  $\sigma_7 = 0.20$ ,  $\sigma_8 = 0.27$ , are again small, while the errors of the velocity-dispersion parameters are much larger:  $\sigma_2 = 2.9 \times 10^4 \text{ km}^2/\text{s}^2$ ,  $\sigma_3 = 8.1 \times 10^4 \text{ km}^2/\text{s}^2$ ,  $\sigma_4 = 3.4 \times 10^3 \text{ kpc}$  and  $\sigma_5 = 4.7 \times 10^3 \text{ kpc}$  (the degenerate parallax errors are, again, only insignificantly larger).

The diagonalisation procedure used above for the CS case gives for the eigenvectors mixing the velocity-dispersion parameters  $\sigma_{(2)} = 0.30$ ,  $\sigma_{(3)} = 207$ ,  $\sigma_{(4)} = 183$  and  $\sigma_{(5)} = 1100$ . Although the three eigen-errors  $\sigma_{(3)}$ ,  $\sigma_{(4)}$  and  $\sigma_{(5)}$  seem inordinately large, the corresponding shifts  $\sigma_{(i)}\mathbf{V}_{(i)}$  in the parameter space do not produce dramatic changes in the structure of the halo. Table 2 gives the values of the halo parameters after these shifts, as well as the radial and tangential velocity dispersions. Not surprisingly, in all three cases the very large magnitudes of  $r_o$  and  $l$  ensure position-independent velocity dispersion profiles and through very different combinations of  $\sigma_o$  and  $\sigma_+$  lead to  $\sigma_r$  and  $\sigma_t$  relatively close to those of SIS. This ‘degenerate’ (almost) SIS structure shows even more clearly than the above CS-based example that large uncertainties in the values of the halo parameters are not incompatible with a good grasp of the structure of the halo: parallax microlensing can probe the halo while ignoring the vagaries of our parametrisation of its structure.

## 6 CONCLUSION

The use of parallax microlensing for the class of models discussed in this paper indeed brings a great advantage: it allows an effective disentanglement of the mass function of the MHOs and the structure of the halo. There indeed seems to be a way to go beyond the somewhat pessimistic conclusions of paper I and infer accurately the average mass of the MHOs (together with the shape of the mass function) after detecting a realistic number,  $N \sim 100$ , of events. In addition, one can constrain the halo structure much more tightly than it is possible through measurement of event durations only.

Moreover, some combinations of parameters describing the halo structure can be inferred rather accurately. Virtually all the uncertainty regarding the halo model is then localised in a few (precisely *one* in the CS-based example discussed in Section 5) ‘eigen-modes’ of the halo, i.e., those displacements in the halo parameter space that are left ‘loose’ by parallax microlensing while allowing other displacements to be independently (and tightly) constrained. These poorly constrained modes correspond to particularly small changes in the *actual* structure of the halo as given by density and velocity dispersion profiles. Unfortunately, their large associated eigen-errors may push us into a non-linear regime (inadequately charted by the Cramer limit) of deviations in the halo structure that can be properly explored only by time-consuming Monte-Carlo simulations.

Although obtained on the basis of a limited class of halo models, the above conclusions should be relevant in a broader context. The halo structure/mass function disentanglement (and consequently accurate mass determination) as well as the inference of some properties of the halo structure itself should result from the significant enhancement of information (as elaborated in Section 5) due to parallax microlensing even if one allows for a much wider range of halo structures. For instance, in the more general case of non-spherical haloes, one may hope to constrain the density and velocity dispersions *along the line of sight* well enough to determine the mass function. The ‘uncertain’ modes would then describe possibly large changes in the halo structure away from the line of sight. Only parallax microlensing observations in several directions would presumably suffice to infer the overall structure of the halo. These conjectures need to be tested on other, more realistic or better dynamically founded models (e.g., those of Evans 1994) of the halo than the ones discussed in the present paper.

## Acknowledgements

The author thanks Jesper Sommer-Larsen of TAC for numerous enlightening discussions and gratefully acknowledges hospitality of the Aspen Center for Physics, where the earliest version of this paper was conceived. This research was generously supported by Danmarks Grundforskningsfond through its establishment of the Theoretical Astrophysics Center.

## REFERENCES

- Axelrod, T. 1997, Seminar at the Center for Physics, Aspen, June 1997
- Alcock, C. *et al.* 1996, astro-ph/9606165
- Binney, J. & Tremaine, S., 1987, Galactic Dynamics. Princeton Univ. Press, Princeton
- Boutreux, T. & Gould, A. 1996, Ap. J. 462, 705
- Cramer, H., 1946, Mathematical Methods of Statistics. Princeton Univ. Press, Princeton
- Evans, N.W. 1994, MNRAS 267, 333
- Evans, N.W. 1997, astro-ph/9611162
- Gould, A. 1994a, Ap. J. 421, L71
- Gould, A. 1994b, Ap. J. 421, L75
- Gould, A. 1995, Ap. J. 441, L21
- Grieger, B., Kayser, R., & Refsdal, S. 1986, Nature 324, 126
- Greist, K. 1991, Ap. J. 366, 412

- Han, C. & Gould, A. 1995, Ap. J. 447, 53  
 Jones, B.F., Klemola, A.R. & Lin, D.N.C. 1994, Astr. J. 107, 1333  
 Kroupa, P. & Bastian, U. 1997, New Astr. 2, 77  
 Maoz, D. & Gould, A., 1994, Ap. J. 425, L67  
 Markovic, D. & Sommer-Larsen, J., 1997, MNRAS 288, 733; astro-ph/9609187  
 Mihalas, D. & Binney, J., 1981, Galactic Astronomy. Freeman, San Francisco  
 Nemiroff, R.J. & Wickramasinghe, W.A.D.T., 1994, Ap. J. 424, L21  
 Sommer-Larsen, J., Flynn C. & Christensen, P.R., 1994, MNRAS 271, 94  
 Sommer-Larsen, J., Beers, T.C, Flynn C., Wilhelm, R. & Christensen, P.R., 1997, Ap. J. 481, 775

### Appendix: Position and motion of the Earth relative to the Galaxy and the Large Magellanic Cloud

This appendix contains formulae (with derivations) giving positions and proper motions in the rest frame of the Galaxy of points along the Earth-Large Magellanic Cloud line of sight.

We denote by  $\hat{\mathbf{x}}$ ,  $\hat{\mathbf{y}}$  and  $\hat{\mathbf{z}}$  unit vectors directed, respectively, toward the Galactic centre (GC), tangentially along the rotation of the ‘local standard of rest’ (LSR) around the galactic centre, and toward the north Galactic pole. If the velocity of a source relative to the Sun is given in terms of Galactic-coordinate components  $v_{\text{rad}}$ ,  $v_l$  and  $v_b$ , the conversion to the  $x$ ,  $y$ ,  $z$  components is

$$\begin{aligned} \mathbf{v}'_{\text{s}} = & (\cos b \cos l v_{\text{rad}} - \sin b \cos l v_b - \sin l v_l) \hat{\mathbf{x}} \\ & + (\cos b \sin l v_{\text{rad}} - \sin b \sin l v_b + \cos l v_l) \hat{\mathbf{y}} \\ & + (\sin b v_{\text{rad}} + \cos b v_b) \hat{\mathbf{z}} \end{aligned} \quad (\text{A1})$$

in the rest frame of the Sun. From the 1990 data of B. Jones (as quoted in Greist 1991) the proper motion of the LMC is

$$\begin{aligned} v_{\text{rad}} &= 250 \pm 5 \text{ km/s} \\ v_b &= 335 \pm 62 \text{ km/s} \\ v_l &= -31 \pm 62 \text{ km/s.} \end{aligned} \quad (\text{A2})$$

Disregarding the error bars and using  $D = 55 \text{ kpc}$ ,  $b = -32^\circ.8$ ,  $l = 281^\circ$ , [thus  $\mathbf{r}_{\text{LMC}} = D\hat{\mathbf{k}} = 55 \text{ kpc} (0.160, -0.825, -0.542)$ ;  $\hat{\mathbf{k}} \cdot \hat{\mathbf{k}} = 1$ ] we arrive at  $\mathbf{v}'_{\text{LMC}} = (44, -390, 146) \text{ km/s}$ . Bearing in mind that the Sun’s velocity relative to the Galaxy is  $\mathbf{v}_{\odot} = (0, 220, 0) + (9, 11, 16) = (9, 231, 16) \text{ km/s}$ , where the first and second terms are the velocity of LSR relative to the Galaxy and that of the Sun relative to LSR, the velocity of the LMC relative to the Galaxy is

$$\mathbf{v}_{\text{LMC}} = \mathbf{v}_{\odot} + \mathbf{v}'_{\text{LMC}} = (53, -159, 162) \text{ km/s.} \quad (\text{A3})$$

[After completing the calculations described in this paper, the author learned about more recent values of Jones, Klemola & Lin (1994) who give  $\mathbf{v}_{\text{LMC}} = (60 \pm 59, -155 \pm 25, 144 \pm 51) \text{ km/s}$ . On the other hand, Kroupa & Bastian (1997) give an estimate based, among other sources, on the Hipparcos data:  $\mathbf{v}_{\text{LMC}} = (41 \pm 44, -200 \pm 31, 169 \pm 37) \text{ km/s}$ . These values do not differ sufficiently from velocity (A3) to lead to a significant change in the results reported in this paper.]

Along the Sun-LMC line of sight we can introduce auxiliary coordinates defined by the following orthonormal system: as above,  $\hat{\mathbf{k}}$  is directed along the line of sight,  $\hat{\mathbf{i}}$  lies in the Sun-GC-LMC plane and points in the direction of the GC and  $\hat{\mathbf{j}} = \hat{\mathbf{k}} \times \hat{\mathbf{i}}$ . Given the data listed above,  $\hat{\mathbf{i}} = (0.987, 0.134, 0.088)$  and  $\hat{\mathbf{j}} = (0, -0.549, 0.836)$ . Each point on the line of sight moves relative to the galaxy with velocity  $\mathbf{s}(z) = \mathbf{v}_{\odot}(1-z) + \mathbf{v}_{\text{LMC}}z$  whose components along  $\hat{\mathbf{i}}$  and  $\hat{\mathbf{j}}$  are

$$\begin{aligned} s_i &= v_{\odot_i}(1-z) + v_{\text{LMC}_i}z \\ s_j &= v_{\odot_j}(1-z) + v_{\text{LMC}_j}z, \end{aligned} \quad (\text{A4})$$

where  $v_{\odot_i} = 41 \text{ km/s}$ ,  $v_{\text{LMC}_i} = 45 \text{ km/s}$ ,  $v_{\odot_j} = -113 \text{ km/s}$  and  $v_{\text{LMC}_j} = 223 \text{ km/s}$ .

In the above we have neglected the motion (revolution) of the Earth (detector ‘1’) and the satellite (detector ‘2’) around the Sun: one should in principle add the term  $\boldsymbol{\omega} \times \mathbf{r}_{\oplus}$  (or the corresponding term for the satellite) to  $\mathbf{v}_{\odot}$ . To avoid (at this stage) unnecessary complication we will keep disregarding the revolution around the Sun. For specific computations in this paper we assume that the ‘1’-‘2’ line points along the unit vector  $\hat{\mathbf{r}}$  directed along  $\hat{\boldsymbol{\omega}} \times \hat{\mathbf{k}}$ . Since in galactic coordinates  $\hat{\boldsymbol{\omega}} = (-0.095, 0.862, 0.498)$ , (derived from data in Mihalas & Binney 1981) we find  $\hat{\mathbf{r}} = (-0.652, 0.324, -0.685)$  and thus  $\hat{\mathbf{r}} \cdot \hat{\mathbf{i}} = -0.660 = \cos \phi_o$  and  $\hat{\mathbf{r}} \cdot \hat{\mathbf{j}} = -0.750 = \sin \phi_o$  corresponding to  $\phi_o = 229^\circ$ .